RSC Advances

PAPER

View Article Online
View Journal | View Issue

Cite this: *RSC Adv.*, 2026, **16**, 26438

Validating free spectral range tracking as a robust method for mitigating artifacts in VSC kinetics

Kaihao Gu, †[a] Xinmin Zhao,†[a] Runling Peng*[a] and Feng Zhang *[ab]

Vibrational strong coupling (VSC) has been reported to modify ground-state chemical reactivity; however, quantitative interpretation of cavity-controlled kinetics depends critically on the spectroscopic observable used to extract rate constants. Here, we systematically compare two commonly employed cavity readout strategies—single-mode frequency shifts (Δf) and free spectral range variations (ΔFSR)—using the VSC-modulated deprotection of 1-phenyl-2-trimethylsilylacetylene (PTA) as a benchmark reaction. Reaction kinetics were monitored in real time inside a Fabry–Pérot cavity, and rate constants were extracted using a normalized first-order formalism. We show that single-mode tracking is sensitive to thermal drift and global cavity perturbations, leading to systematic deviations in the extracted rate constant even for small temperature variations ($\Delta T = 1$ K). Under VSC conditions, ΔFSR-based analysis yields a reaction rate suppression factor of approximately 5.1 relative to the non-cavity case, whereas Δf-based analysis reports only ~4.25-fold suppression. This discrepancy reflects the higher susceptibility of single-mode observables to non-reactive perturbations. These results demonstrate that differential cavity observables provide improved quantitative reliability for kinetic analysis under VSC and emphasize the importance of rigorous methodological validation in cavity-controlled chemistry.

Received 2nd March 2026
Accepted 13th May 2026

DOI: 10.1039/d6ra01794k

rsc.li/rsc-advances

Introduction

Polaritonic chemistry, the control of chemical reactivity by tuning the surrounding electromagnetic environment, represents a new frontier in chemistry.[1–3] A particularly promising paradigm has emerged in the form of Vibrational Strong Coupling (VSC), where the collective coupling of molecular vibrations to the vacuum field of an optical microcavity creates new hybrid light-matter states known as vibrational polaritons. This non-invasive method modifies the molecular potential energy landscape, thereby offering a novel handle to alter ground-state chemical reactivity.[4–10] Since the pioneering work by Ebbesen and coworkers demonstrated a significant modification of a Si–C bond cleavage rate under VSC,[3] the field has expanded rapidly to showcase control over a wide array of chemical processes, including catalysis,[3,11,12] enzymatic activity[13] and mode selectivity.[2,14–19] Recent studies have further delved into the nuanced dependencies of this effect, exploring, for example, how the choice of the coupled vibrational mode can dramatically influence thermodynamic parameters and reaction outcomes.[20–23]

Accurate *in situ* monitoring of reaction kinetics is paramount for deciphering the underlying mechanisms of VSC. Two main approaches based on Fabry–Pérot (FP) cavity transmission have been employed for this purpose. One method tracks the frequency shift (Δf) of a single, high-order detuned mode,[24–27] while the other tracks the change in the Free Spectral Range (FSR) between two or more modes. Both methods are premised on the principle that changes in the intracavity medium's refractive index, caused by reactant consumption, will alter the optical path length and thus the spectral features. However, despite the concurrent use of these two approaches in the literature, a systematic comparison of their reliability and potential discrepancies under VSC conditions has been notably absent, and the choice of method often appears arbitrary.

However, several recent reports suggest that the effects of VSC should be re-examined,[14,21,23,28,29] making the need for such a critical evaluation increasingly urgent. Recent work has begun to highlight the susceptibility of FP-based measurements to various artifacts.[23,29] More fundamentally, a theoretical understanding has emerged that VSC itself introduces a global change to the cavity's dielectric environment, an effect that would differently impact single-mode tracking *versus* ratiometric tracking like FSR.[23,30] This raises a critical, unaddressed question: are the Δf and ΔFSR methods truly interchangeable, or does one possess an inherent robustness that the other lacks? Recent meticulous studies have implicitly acknowledged these

[a]*Terahertz Technology Innovation Research Institute, Terahertz Spectrum and Imaging Technology Cooperative Innovation Center, Shanghai Key Lab of Modern Optical System, School of Optical-Electrical and Computer Engineering, University of Shanghai for Science and Technology, Shanghai 200093, China. E-mail: fzhang@usst.edu.cn*

[b]*Zhejiang Key Laboratory of Soft Matter Biomedical Materials, Wenzhou Institute, University of Chinese Academy of Sciences, Wenzhou, Zhejiang 325000, China*

† These authors contributed equally to this work.

challenges by calling for more rigorous calibration,[23] yet they stop short of a direct, comparative dissection of the methods themselves.

In this work, we directly investigate the potential optical artifacts present in two *in situ* tracking methods. We provide the first systematic, experimental deconstruction and comparison of the Δf and FSR kinetic tracking methods within the context of VSC. We first systematically quantify two major sources of potential error—macroscopic thermal drift and the intrinsic, coupling-induced spectral artifact—and analyze their differential impact on each method. By conducting a comparison, we demonstrate that the single-mode Δf tracking method suffers from significant nonlinearity and can introduce systematic bias in the extracted rate constant. Conversely, we provide clear experimental validation that FSR tracking effectively mitigates these artifacts, yielding superior linearity and accuracy. Our results resolve the long-standing ambiguity regarding the choice of kinetic probe and establish a clear, evidence-based guideline for reliable quantitative analysis in polaritonic chemistry.

Experimental

Materials

The 1-phenyl-2-trimethylsilylacetylene (PTA) (98.5%), tetra-*n*-butylammonium fluoride (TBAF), methanol (anhydrous, 99.5%) and heavy water (D_2O, 99.9 atom % D) were procured from Sigma-Aldrich (Merck Co., Ltd, Shanghai, China). A stock solution of TBAF (3 M) was prepared in methanol. PTA was dissolved in methanol to obtain the desired initial concentration at 3.33 M. All chemicals were used as received without further purification.

Fabry–Pérot cavity assembly and characterization

The FP cavity was assembled by sandwiching a Teflon spacer between the two gold-coated CaF_2 mirrors. The mirrors consisted of CaF_2 substrates coated with a 10 nm Au reflective layer and subsequently covered with a 100 nm SiO_2 insulating layer. The cavity length was defined by Teflon spacers of varying thickness. This assembly was then mounted in a demountable liquid cell. The cavity was filled with the sample liquid (*e.g.*, H_2O, D_2O, or PTA solutions) *via* injection into the cell ports. The optical path length (L) of the cavity was not measured mechanically but was precisely determined *in situ* from the transmission spectrum of the cavity filled with a neat solvent of known refractive index (n). The FSR, which is the frequency spacing between adjacent cavity modes (m and $m+1$), was used to calculate L according to the formula:

$$L(\mu\text{m}) = \frac{10^4}{2n \times \text{FSR}(\text{cm}^{-1})} \quad (1)$$

Spectroscopic measurements

All transmission spectra were recorded using a Nicolet IS 5 Fourier-transform infrared (FTIR) spectrometer. Unless otherwise specified, all spectra were recorded at a controlled temperature of 25 ± 0.1 °C. For each spectrum, 36 scans were co-added at a resolution of 0.2 cm^{-1}.

Experimental procedures

Thermal drift measurements. A cavity filled with neat H_2O/D_2O/PTA at room temperature was placed into the sample compartment of the FTIR spectrometer with specific temperature. Transmission spectra were recorded immediately and subsequently at 5 minute intervals for a total duration of 4 hours to monitor the frequency drift of the cavity modes and the FSR.

Coupling-induced artifact measurements. FP cavities of different lengths were filled with D_2O. The cavity lengths were specifically chosen such that the O–D stretching vibration of D_2O (~2500 cm^{-1}) was brought into resonance with different cavity modes (m = 1 to 8). For each cavity, a full transmission spectrum was recorded to analyze the frequency shifts of all high-order, detuned modes.

Calibration curve measurements. A series of standard PTA solutions with concentrations ranging from 0.02 to 3.0 M were prepared by serial dilution of the stock solution. The cavity was first filled with pure methanol to obtain a reference spectrum (C_{PTA} = 0 M). Subsequently, the cavity was filled with each standard solution in order of increasing concentration. After each measurement, the cavity was thoroughly flushed with pure methanol and dried with a stream of nitrogen gas to prevent cross-contamination.

PTA deprotection reaction

The desilylation of PTA was performed in methanol using TBAF as the fluoride source. The reaction was initiated by adding 10 μL of the TBAF (3 M) stock solution to 90 μL PTA (3.33 M) solution under vigorous mixing to ensure homogeneity. The reaction proceeds *via* fluoride-induced cleavage of the trimethylsilyl group to yield the corresponding terminal alkyne. The reactant and product exhibit slightly different refractive indices, enabling kinetic monitoring through changes in the optical response of the reaction medium.

For kinetic analysis, the reaction progress was followed in real time by tracking the temporal spectral shift of a selected optical mode. The maximum spectral shift corresponding to complete conversion ($\Delta\infty$) was determined independently from control experiments. The completion point was defined from an independently prepared endpoint sample with the same final solvent and reagent composition, after the reaction was allowed to proceed until no further measurable spectral shift was observed. Assuming apparent first-order conditions, the rate constant was extracted from the linear fit of $\ln(1 - \Delta S_t/\Delta S_{inf}) = -kt$.

Data analysis

All spectral data were processed using custom scripts written in Origin. The precise positions of the cavity modes (f_m) were determined by fitting the transmission peaks to a Lorentzian function to find the peak. Unless otherwise specified, ΔFSR was extracted from two adjacent high-order cavity modes located above 6000 cm^{-1} to minimize perturbation from molecular

absorption and coupling-induced dispersion (*e.g.*, FSR = $f_{m+1} - f_m$).

The relative shifts, $\Delta f/f_0$ and $\Delta\mathrm{FSR}/\mathrm{FSR}_0$, were calculated with respect to the values obtained from the neat solvent (f_0 and FSR_0). Linear regression analysis of the calibration data was performed using the linearfit function from Origin. The key statistical parameters, including the slope, the coefficient of determination (R^2), and the standard deviation of the residuals, were extracted directly from the fitting results. The percentage of rate underestimation was calculated as $|k_{\mathrm{FSR}}/k_{\mathrm{f}} - 1| \times 100\%$, where k_{FSR} and k_{f} are the slopes of the respective calibration curves.

The reaction kinetics were extracted using a normalized spectral-response formalism applicable to both cavity observables employed in this work. The time-dependent signal shift, denoted as ΔS_{t}, represents either Δf or $\Delta\mathrm{FSR}$. The maximum signal change at reaction completion, ΔS_{inf}, was determined independently from control measurements.

Under apparent first-order conditions, the reaction progress can be expressed in terms of the fractional conversion, which is proportional to the normalized spectral response: $\ln(1 - \Delta S_t/\Delta S_{\mathrm{inf}}) = -kt$.

The rate constant k was obtained from the slope of the linear fit of the semi-logarithmic plot. Importantly, this normalization procedure eliminates trivial proportional scaling differences between observables and ensures that both Δf- and $\Delta\mathrm{FSR}$-based analyses probe the same underlying kinetic process.

Results and discussion

The experimental concept and analytical methodology investigated in this work are schematically outlined in Fig. 1. At the

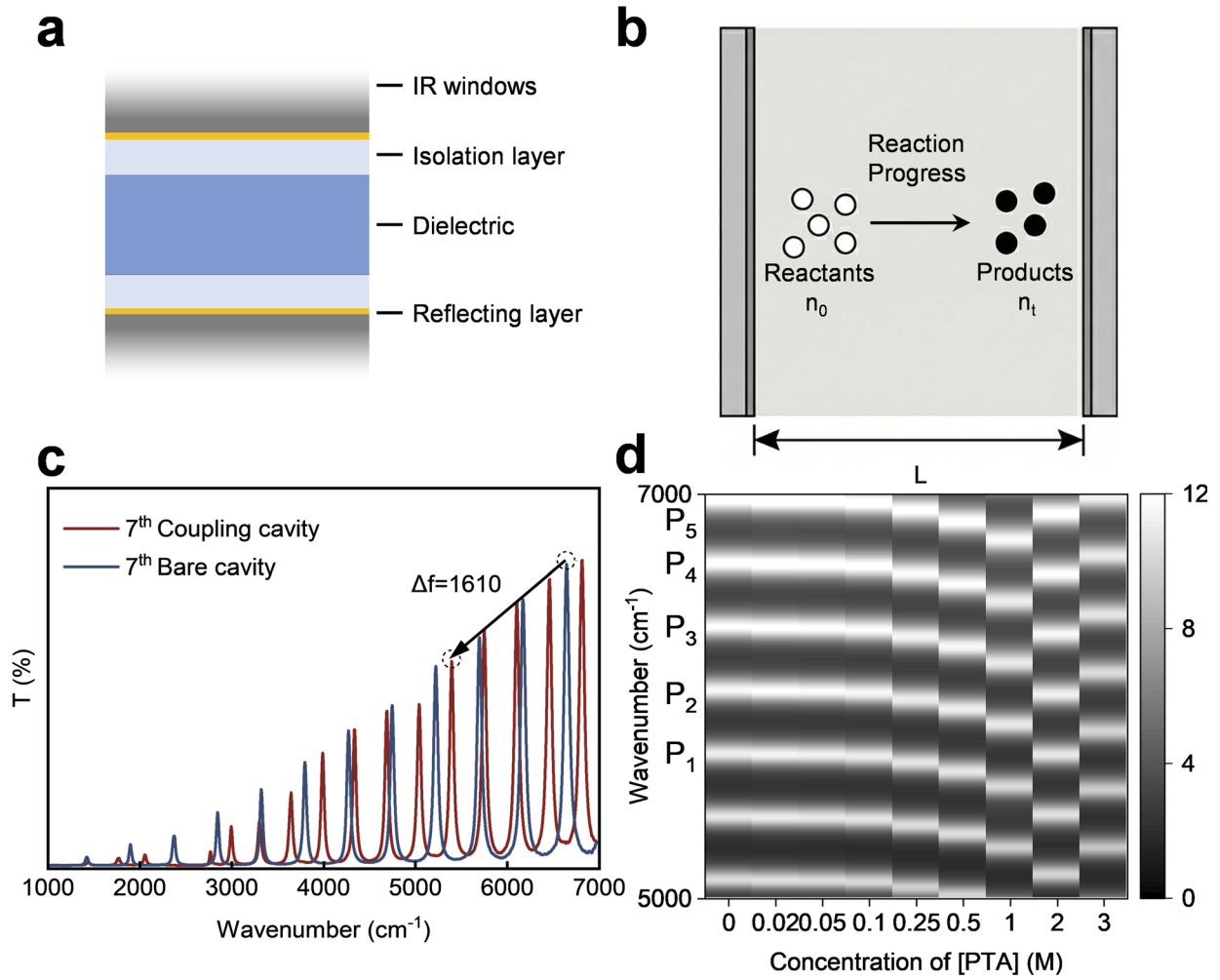

Fig. 1 Structural design and optical response of the Fabry–Pérot cavity under VSC. (a) Schematic illustration of the FP cavity structure. The IR windows are typically fabricated from infrared-transparent materials such as CaF_2 or ZnSe. The isolation layer is formed by spin-coating or vapor deposition of a chemically inert material that does not react with the solvent or substrate under study; commonly used materials include PMMA, PVA, PDMS, or SiO_2. The reflective layer consists of highly reflective metals such as Au or Ag. (b) During a reaction under VSC, the transformation from substrate to product induces a change in refractive index within the cavity medium. (c) Infrared spectra of the FP cavity mode ($m = 7$) before and after coupling with D_2O. The resonance peak at 6833 cm^{-1} exhibits an apparent shift of approximately 1610 cm^{-1}, corresponding to an apparent refractive index change of ~0.333. (d) Transmission spectra recorded at different PTA concentrations. Beginning at 5000 cm^{-1}, the resonance peaks are labeled sequentially as P_1, P_2, P_3, *etc.*, clearly illustrating the systematic migration of the cavity resonances with increasing concentration.

core of our study is a FP cavity, assembled from two parallel mirrors enclosing the reacting medium, as depicted in Fig. 1a. The central premise of kinetic monitoring is that the reaction-induced change in refractive index alters these spectral features. The conventional approach, conceptually illustrated in Fig. 1b, tracks the frequency shift (Δf) of a single, detuned probe mode. However, this method is susceptible to artifacts. A typical transmission spectrum obtained from this cavity reveals a series of resonant modes superimposed on the absorption profile of the molecular species (Fig. 1c). In contrast, this work validates an alternative method, shown in Fig. 1d, which tracks the change in the FSR—the frequency spacing between two adjacent modes. The following sections will present a systematic, experimental comparison to demonstrate the superior robustness and accuracy of the FSR method.

Resonance drift induced by thermal instability

Before interrogating the intrinsic effects of VSC, it is imperative to assess the baseline stability of the FP cavity platform commonly employed in VSC experiments—specifically, whether the cavity resonance frequencies remain stable under non-reactive conditions. Several routine verification steps are typically performed. After assembling the microfluidic cavity, researchers generally allow the system to rest for approximately 1 hour to achieve pressure equilibration within the cavity.[31] The cavity mode frequencies are then re-measured; if significant deviations are observed, the cavity alignment is readjusted, followed by another equilibration period. This procedure is repeated until the cavity mode frequencies stabilize. Subsequently, the reaction solution is introduced, and after a designated reaction period, the solution is either withdrawn for *ex situ* analysis or monitored *in situ* for kinetic measurements.

Regardless of whether *in situ* or *ex situ* detection is employed, an unavoidable question arises: does the cavity itself undergo changes during the reaction? More specifically, do the resonance peaks shift over time? This issue is particularly critical because the magnitude of VSC-induced effects depends sensitively on cavity detuning and the Rabi splitting energy. Any unintended drift in cavity resonance during the reaction may therefore confound kinetic interpretation. This issue is critical for any kinetic experiment requiring long-term monitoring. Here, we investigate a potentially overlooked source of error—cavity mode drift induced by thermal equilibration—and demonstrate that the resulting deviations are far from negligible.

Under conditions of a small initial temperature difference ($\Delta T \approx 5$ K), we continuously monitored the frequencies of high-order resonant modes in a Fabry–Pérot cavity. As shown in Fig. 2a, the cavity modes exhibited pronounced and persistent drift. A resonance initially located at approximately 5543 cm^{-1} experienced a frequency shift of up to 32.8 cm^{-1} over a 4 h relaxation period, corresponding to a relative change of about 0.59%. In comparison, the corresponding FSR shift was approximately 2 cm^{-1} relative to an initial FSR of about 430 cm^{-1}, corresponding to a relative change of about 0.47%. Although both observables are affected by thermal relaxation, the FSR-based observable exhibits a slightly smaller relative drift and, more importantly, partially suppresses common-mode spectral translations that would directly affect single-mode tracking. In the lower-frequency region ($\sim$850 cm^{-1}), corresponding to the PTA resonance, a blue shift of approximately 4.7 cm^{-1} was observed (Fig. 2b).

When varying the initial temperature difference ($\Delta T = 1$, 3, and 5 K), the resulting Δf_{240} values were 18.3, 25.1, and 32.8 cm^{-1}, respectively, while ΔFSR_{240} amounted to 0.9, 1.7, and 2 cm^{-1} (Fig. 2c). The drift process displays characteristic thermal relaxation behavior, with the most rapid frequency changes occurring within the first hour of measurement (Fig. S1).

These findings reveal a serious and frequently overlooked issue in long-duration kinetic studies. The phenomenon originates from the multi-component thermal exchange dynamics intrinsic to the FP cavity system. An initial temperature gradient establishes a pronounced thermal imbalance between the interior and exterior of the cavity. Since heat conduction rates scale with the magnitude of the temperature gradient, rapid heat exchange occurs *via* thermal conduction and micro-convective flows within the cavity liquid. Moreover, the CaF_2 windows, gold reflective layers, Teflon spacers, and intracavity liquid possess substantially different heat capacities and thermal conductivities. This mismatch results in transient temperature nonuniformity across components, leading to dynamic variations in the effective optical path length. Concurrently, incomplete thermal diffusion within the cavity liquid produces spatial refractive index inhomogeneity, further amplifying resonance frequency fluctuations. As thermal relaxation proceeds, the temperature gradient diminishes, the components reach thermal equilibrium, the refractive index regains spatial uniformity, and the rate of frequency drift correspondingly slows.

A frequency drift as large as 30 cm^{-1}, if mistakenly attributed to reaction progress, would introduce substantial quantitative inaccuracies. This issue is even more difficult to avoid in experiments conducted under nominal "room temperature" conditions. We therefore examined the high-order mode drift of an empty cavity left under ambient laboratory conditions during natural day–night temperature fluctuations. As the temperature varied from 295 K to 299 K and subsequently to 296 K, cumulative frequency deviations of up to $\sim$30 cm^{-1} were observed (Fig. 2d). These results indicate that strict thermal equilibration before kinetic measurements is necessary. To further evaluate the cavity stability after thermal equilibration, we monitored the cavity-mode drift of multiple independent microcavities over 4 h before and after PTA injection (Fig. S2–S4). As summarized in Table S1, the maximum drift after PTA injection was 2.1208 cm^{-1} over 240 min, which is much smaller than the drift observed under non-equilibrium thermal relaxation or uncontrolled ambient-temperature fluctuation. These results demonstrate that, after sufficient thermal equilibration, the microcavity exhibits good stability over the timescale relevant to the kinetic measurements.

To illustrate the quantitative consequence, in experiments tracking the reaction of PTA, an FSR shift of merely 2 cm^{-1}

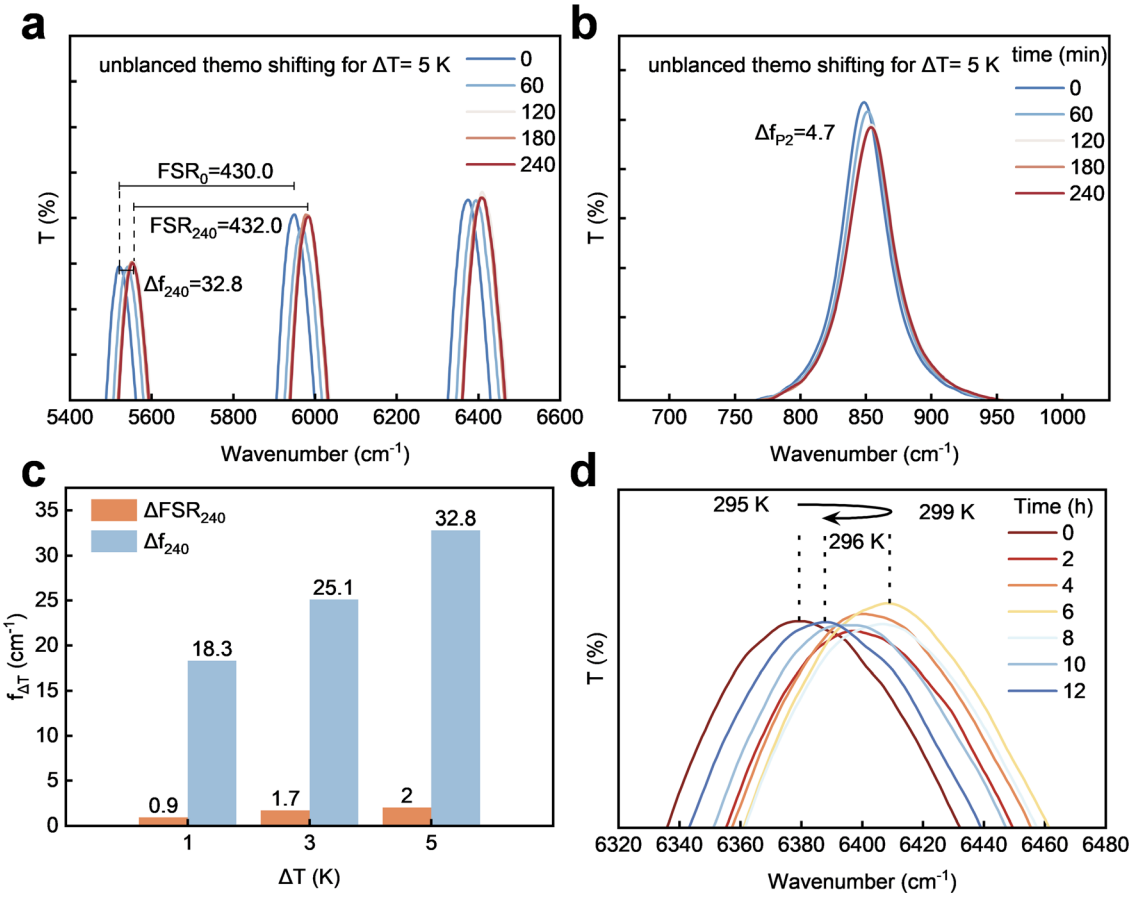

Fig. 2 Thermal relaxation–induced cavity drift and equilibration behavior. (a) Thermal relaxation–induced frequency drift of the $m = 10$ cavity mode under nonequilibrium conditions with $\Delta T = 5$ K, monitored over 240 min. The resonance exhibits a maximum FSR shift of approximately 2 cm^{-1} and a total frequency drift Δf of 32.8 cm^{-1}. (b) Thermal relaxation–induced drift of the $m = 2$ cavity mode under $\Delta T = 5$ K over 240 min, yielding a frequency shift of $\Delta f_{P2} = 4.7$ cm^{-1}. (c) Frequency deviations ($f_{\Delta T}$) arising from thermal drift within a 240 min time window under different initial temperature differences ($\Delta T = 1$, 3, and 5 K). (d) Cavity equilibration process over 12 h under ambient room-temperature conditions, illustrating resonance drift driven by natural environmental temperature fluctuations.

corresponds to a concentration reading error as large as 0.16 M. These results strongly indicate that any method relying on the absolute frequency of a single resonance peak (Δf) is highly susceptible to environmental thermal fluctuations, thereby calling its reliability into question. Accordingly, a measurement strategy capable of intrinsically compensating for resonance mode drift is a prerequisite for obtaining trustworthy kinetic data. Before interrogating more subtle coupling-induced effects, it is therefore essential to identify a methodology that can inherently suppress such macroscopic thermal drift.

Global influence of coupling on cavity modes

Beyond external environmental perturbations, we further investigated a deeper, intrinsic measurement artifact arising from the VSC effect itself. Recent theoretical work by Thomas[23] predicts that the formation of strong light–matter coupling modifies the dispersion relation of the intracavity medium over a broad spectral range, thereby inducing global blue or red shifts in all cavity modes, depending on their relative detuning with respect to the molecular resonance. The present study provides direct experimental validation of this theoretical prediction.

We constructed systems in which the O–D stretching vibration of D_2O (~2500 cm^{-1}) was resonantly coupled to cavity modes of different orders ($m = 1$–8) (Fig. S5). We then precisely measured the apparent refractive index variation of highly detuned "probe" modes located far from the coupling region (>3000 cm^{-1}), expressed as $\Delta f/f_0$. As shown in Fig. 3a, even these strongly detuned resonances exhibited systematic frequency shifts induced by strong coupling in the low-frequency region. The resonance frequency positions are intrinsically and globally correlated with the light–matter coupling strength inside the cavity. The magnitude of the shift is more pronounced for modes closer to the coupling region and gradually approaches a stable but nonzero plateau as the probe frequency increases.

We further examined probe modes in the mid-high-frequency (>5000 cm^{-1}) and high-frequency (>6000 cm^{-1}) regions. When $\Delta f/f_0$ was used for quantitative detection and a probe frequency in the >5000 cm^{-1} region was selected, the standard deviation (SD) reached 0.0033, corresponding to a systematic deviation of approximately 20 cm^{-1} for a resonance

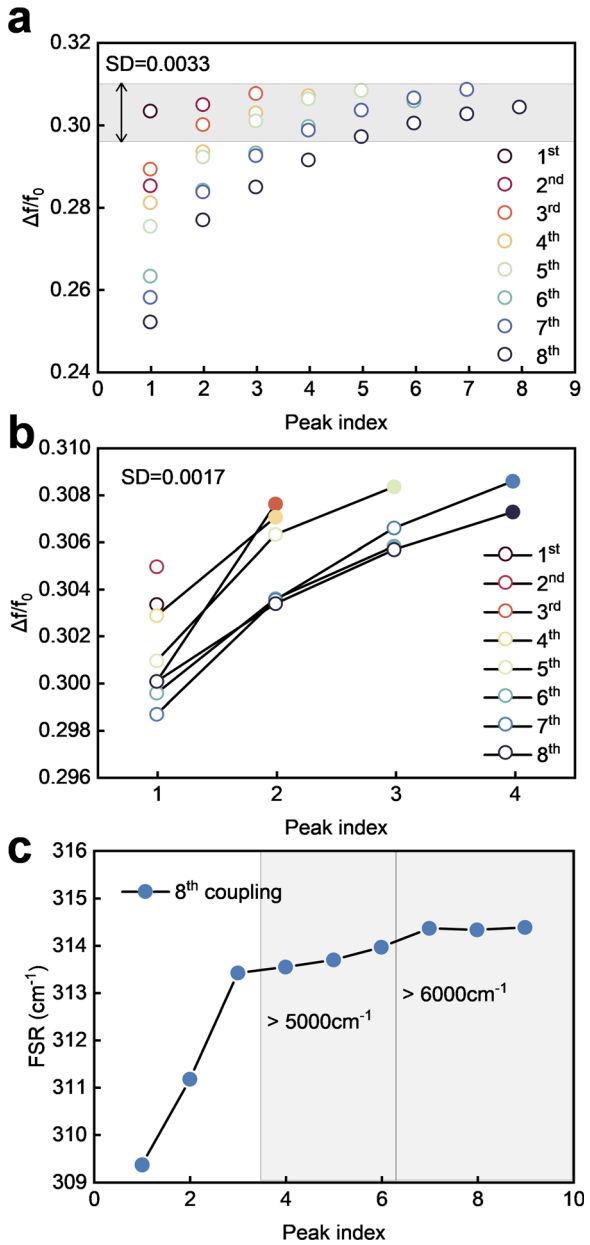

Fig. 3 Apparent refractive index extraction using single-mode tracking and differential FSR analysis. (a) Apparent refractive index changes of D_2O stretching vibrations coupled with the 1st to 8th modes of the FP cavity, extracted *via* Δf. Different colors correspond to apparent refractive indices extracted from the high-frequency region above 3000 cm^{-1} for each coupling order. The *x*-axis represents the peak index from low to high frequency. (b) Apparent refractive index changes of D_2O stretching vibrations coupled with the 1st to 8th FP modes, extracted *via* Δf. Different colors indicate data from the high-frequency region above 5000 cm^{-1}, and solid circles represent apparent refractive indices above 6000 cm^{-1}. The *x*-axis is the peak index from low to high frequency. (c) FSR changes of D_2O stretching vibrations coupled with the 8th cavity mode, extracted *via* ΔFSR. Peaks closer to higher frequencies correspond to larger FSR values. For resonances above 5000 cm^{-1}, FSR remains stable, with $\Delta FSR/FSR_0$ standard deviation of 5.11252×10^{-4}. For peaks above 6000 cm^{-1}, FSR is fixed at 314.36 cm^{-1}, with $\Delta n/n$ standard deviation of 6.04595×10^{-5}.

near 5000 cm^{-1}. When probe modes of high-frequency region were selected, the SD decreased to 0.0017 (corresponding to ~10 cm^{-1}) (Fig. 3b).

These results indicate that coupling-induced dispersion effects, combined with refractive index inhomogeneity of the solution, can introduce significant systematic errors in reactions involving small refractive index changes. In general, such errors can be mitigated by selecting higher-frequency probe modes that are further removed from regions of strong dielectric dispersion. The quantitative concentration error scales with the overall apparent refractive index of the reacting system; for a medium with an apparent refractive index of 1.20, the resulting quantitative deviation is on the order of ~0.002 in relative refractive index.

We performed analogous experiments by coupling the O–H stretching vibration of H_2O (~3400 cm^{-1}) to cavity modes with different orders (m = 1–8). Because of the combination bands associated with O–H stretching and bending vibrations, a weak absorption feature appears near 5600 cm^{-1}, which perturbs the probe modes located in this spectral region. According to the Kramers–Kronig relations, this absorption feature is accompanied by a local dispersive change in the real part of the refractive index, thereby affecting the apparent positions of nearby probe modes. In contrast, the corresponding air-filled empty cavities designed for these coupling conditions exhibit excellent FSR consistency across different cavity orders (Fig. S6). This comparison indicates that the apparent variation observed near 5600 cm^{-1} does not arise from cavity fabrication or mode-order-dependent FSR mismatch, but from the intrinsic absorption–dispersion response of the H_2O-filled cavity system. Consequently, when water is used as a solvent in VSC experiments, this combination band near ~5600 cm^{-1} can significantly perturb probe modes in that wavenumber range, leading to apparent refractive index measurement bias. In practice, probe modes above 6000 cm^{-1} should therefore be preferentially selected. If experimental constraints require operation near 5600 cm^{-1}, water should be avoided as the reaction solvent to eliminate interference from combination-band absorption.

Given that the study on the frequency-shift quantification method demonstrated that probe modes in the high-frequency region exhibit better stability, we subsequently investigated the quantitative stability of using FSR as a sensing metric across different spectral regions. As shown in Fig. 3c, when ΔFSR is used as the observable to analyze the high-frequency probe modes after coupling the D_2O stretching vibration with the 8th cavity mode, FSR extracted from different high-frequency regions still exhibits certain quantitative differences. Overall, peaks located closer to the higher-frequency side correspond to larger FSR values, indicating that even far away from the main coupling region, the spacing between probe modes can still be affected by global dispersion renormalization in the strong-coupling system. However, when the probe peaks are selected above 5000 cm^{-1}, the FSR already shows good stability, with a standard deviation of ΔFSR/FSR equal to 5.11252×10^{-4}. When the probe window is further restricted to above 6000 cm^{-1}, the FSR becomes essentially fixed at 314.36 cm^{-1}, and the corresponding standard deviation of $\Delta n/n$ is further

reduced to 6.04595×10^{-5}. These results indicate that although the ΔFSR readout still shows distinguishable regional differences across different high-frequency ranges, selecting probe modes above 6000 cm^{-1} can significantly reduce the quantitative error and is therefore more suitable as a stable and reliable differential probe window for subsequent sensing and kinetic analysis.

According to the Kramers–Kronig relations, any change in molecular absorption during chemical conversion is accompanied by a corresponding dispersive change in the real part of the refractive index. As a result, reaction-induced changes in the composition of the intracavity medium can generate wavelength-dependent refractive-index variations. This effect is most pronounced near molecular absorption bands and becomes weaker in far-detuned spectral regions where the dispersion is smoother. For VSC kinetic studies, this means that the conventional single-mode frequency-shift readout may contain not only the genuine refractive-index change associated with chemical conversion, but also coupling-induced global spectral perturbations arising from changes in collective light–matter coupling strength during the reaction. Because these contributions are superimposed in the absolute frequency shift of a single cavity mode, Δf may not faithfully represent reaction progress without careful calibration or correction. This limitation motivates the use of differential cavity observables, such as ΔFSR, for more robust kinetic analysis.

Methodological benchmarking of FSR tracking

Given that single-mode tracking Δf is simultaneously vulnerable to thermal drift and coupling-induced artifacts, we propose that monitoring the FSR between two high-order modes (>6000 cm^{-1}) constitutes a more reliable quantitative strategy. In principle, because the FSR represents the frequency spacing between adjacent modes, it inherently suppresses common-mode errors that manifest as global spectral translations affecting all resonances similarly.

To directly benchmark the two methodologies, we employed a model system in which the C–Si stretching vibration of PTA (~850 cm^{-1}) was resonantly coupled to the $m = 3$ cavity mode of a Fabry–Pérot cavity. A series of PTA solutions with varying

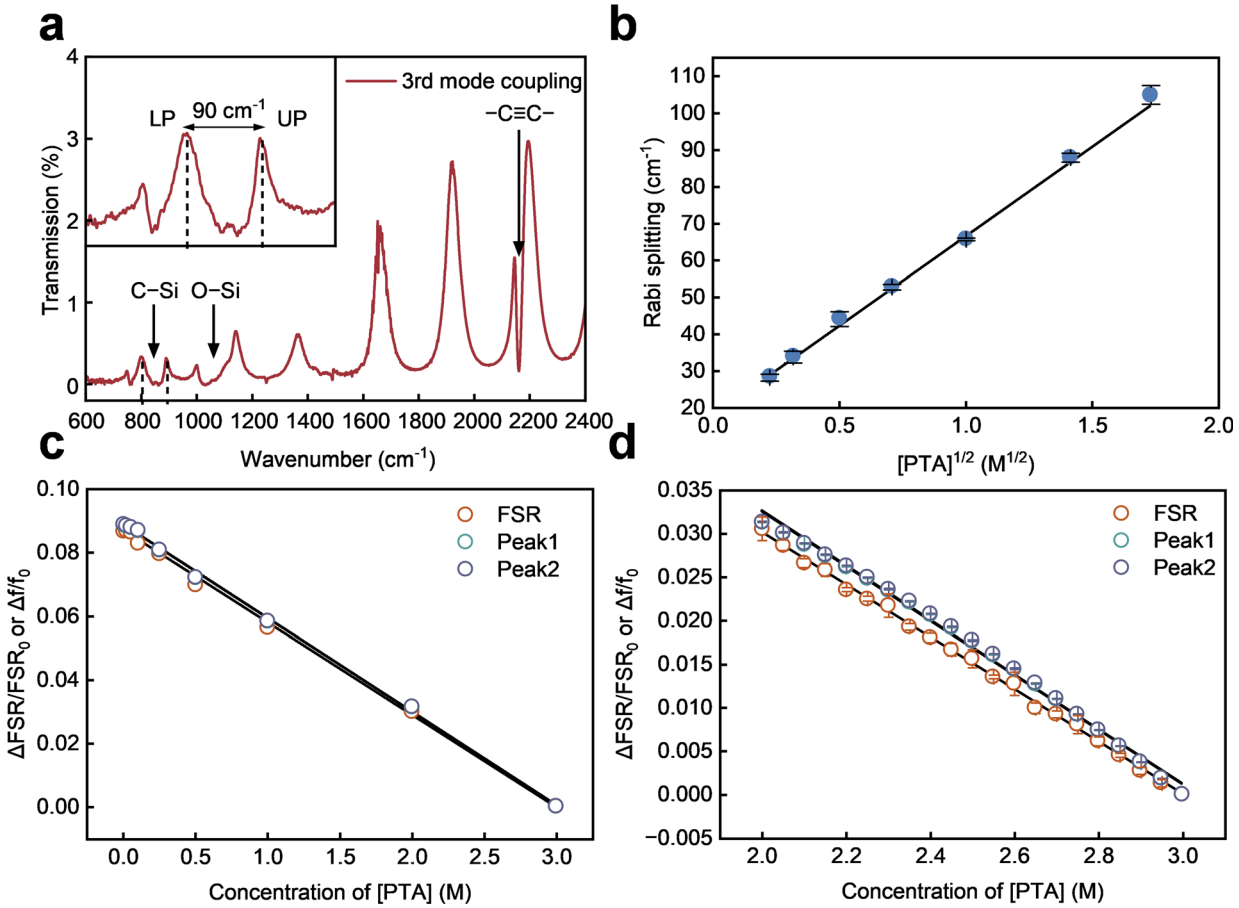

Fig. 4 Strong coupling characterization and concentration-dependent calibration of cavity observables. (a) The 3rd cavity mode coupled with the C–Si resonance of 2 M PTA at 850 cm^{-1}, forming a Rabi splitting with upper and lower polariton branches (UP and LP), resulting in a Rabi splitting width of 90 cm^{-1}. (b) Rabi splitting obtained from the 3rd cavity mode coupled with PTA at different concentrations, showing a linear relationship with $[PTA]^{1/2}$. (c and d) Standard curves of $\Delta FSR/FSR_0$ or $\Delta f/f_0$ *versus* concentration for the 3rd cavity mode coupled with PTA at various concentrations. The slopes correspond to ΔFSR. In a wide concentration range (0.02–3 M) in (c), Peak 1, Peak 2, and ΔFSR have slopes of 0.02914, 0.02952, and 0.02950, respectively. In a narrow concentration range (2–3 M) in (d), the slopes are −0.03013, −0.03143, and −0.03136, with a difference in rate of ~0.0013.

concentrations were prepared, and calibration curves were constructed simultaneously using both Δf and ΔFSR approaches. As shown in Fig. 4a, coupling between the third-order cavity mode and 2 M PTA produced a Rabi splitting of approximately 90 cm^{-1}. The cavity linewidth was 45 cm^{-1}, and the molecular linewidth was 36 cm^{-1}, satisfying the criterion for strong coupling. Moreover, the Rabi splitting exhibited the expected linear dependence on the square root of concentration (Fig. 4b), consistent with strong coupling. Fig. 4c and d present a direct comparison of the two quantification methods. Over a wide concentration range (0.02–3 M), both methods yielded reasonably linear fits. The slopes obtained for ΔFSR, Peak 1, and Peak 2 were 0.02914, 0.02952, and 0.02950, respectively. However, within a narrower concentration window (2–3 M), the slopes became −0.03013, −0.03143, and −0.03136, corresponding to a difference in response rate of approximately 0.0013 M^{-1}. Importantly, Fig. 4d shows that the calibration curve constructed from high-order resonance shifts ($\Delta f/f_0$) exhibits noticeable nonlinearity. As the PTA concentration increases, the coupling strength correspondingly increases, and the probe modes undergo additional nonlinear frequency shifts beyond those arising purely from refractive index variation. This effect distorts the concentration response.

In sharp contrast, the calibration curve based on FSR variation ($\Delta FSR/FSR_0$) demonstrates excellent linearity across the entire concentration range. If researchers were to rely on the conventional $\Delta f/f_0$ method for kinetic calibration and measurement, they would systematically overestimate the true reactant consumption (or product formation) rate by approximately 4.14%. This finding confirms that coupling-induced dielectric modifications indeed perturb resonance-frequency-based quantification. By contrast, FSR-based quantification partially cancels resonance drift errors and corrects the associated systematic deviation, yielding a more faithful representation of concentration changes under VSC conditions.

Benchmarking kinetic readout strategies under VSC

To rigorously assess the quantitative reliability of different spectroscopic observables in cavity-controlled chemistry, we benchmarked two kinetic readout strategies using the well-established VSC-modulated deprotection of PTA. We first examined the susceptibility of cavity-based kinetic analysis to thermal drift. In the absence of active temperature stabilization, even a modest fluctuation of $\Delta T = 1$ K induces a deviation of ~12.5% in the extracted rate constant (Fig. 5a). The corresponding kinetic traces exhibit pronounced deviations from linearity in the semi-log representation, highlighting the intrinsic sensitivity of single-mode frequency tracking to global cavity perturbations. These results underscore that thermal drift is not a secondary correction but a dominant systematic error source in cavity-based kinetic measurements.

We then performed real-time monitoring of the PTA reaction at 3 M under strong vibrational coupling (Fig. 5b). Non-cavity control experiments (≥3 independent runs) yielded a slope of −0.051, consistent with literature values and confirming the intrinsic reproducibility of the reaction system. Under VSC conditions, kinetic analysis based on ΔFSR and Δf readouts yielded slopes of −0.010 and −0.012, respectively. This corresponds to a ~17% discrepancy in the extracted rate constant between the two observables. Using the ΔFSR-derived rate constant, the reaction is suppressed by a factor of 5.1 under VSC relative to the non-cavity case. In contrast, analysis based on Δf underestimates the magnitude of suppression, yielding a factor of only 4.25. Thus, the choice of cavity observable directly alters the quantitative interpretation of vacuum-field-modified reactivity.

The divergence between the two readouts reflects their fundamentally different sensitivities to cavity perturbations. The Δf observable tracks the absolute shift of a single cavity

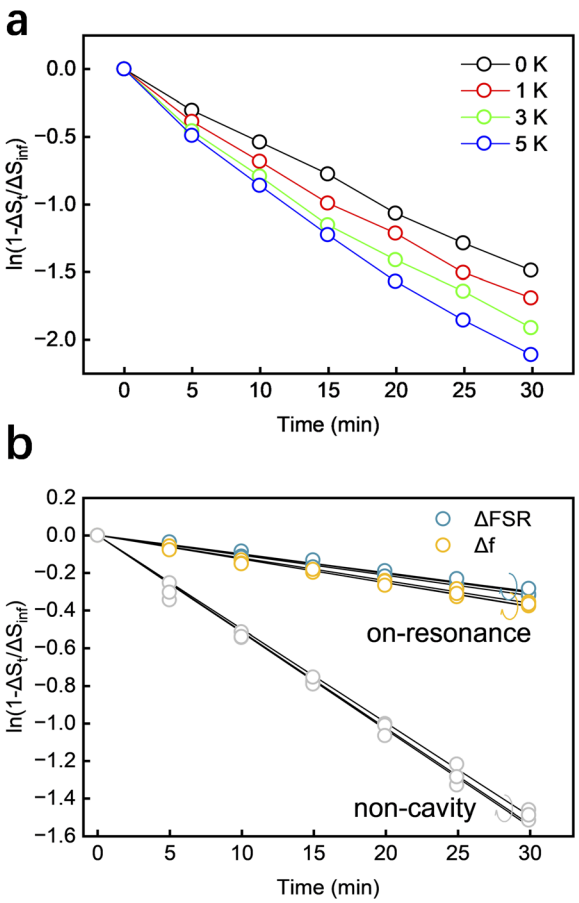

Fig. 5 Kinetic analysis of the PTA deprotection reaction under VSC. (a) Influence of temperature variation on the extracted reaction kinetics inside the cavity. In the absence of active thermal stabilization, even a small temperature difference ($\Delta T = 1$ K) leads to a significant deviation from linear first-order behavior in the semi-logarithmic representation, corresponding to an apparent error of ~12.5% in the rate constant. (b) Real-time monitoring of the PTA reaction under VSC at an initial concentration of 3 M. Rate constants were independently extracted using ΔFSR and Δf readout methods according to the normalized first-order expression. The ΔFSR-based analysis yields a stronger rate suppression (~5.1-fold relative to the non-cavity case) compared to the Δf-based analysis (~4.25-fold), demonstrating that single-mode tracking underestimates the magnitude of VSC-induced reaction suppression. Data were extracted from the temporal shift or FSR variation of a high-order cavity mode.

mode and is therefore susceptible to global spectral translations arising from temperature variations, cavity-length fluctuations, and coupling-induced modifications of the effective dielectric environment. By contrast, ΔFSR represents a differential measurement between adjacent cavity modes. As a consequence, common-mode spectral shifts largely cancel, rendering ΔFSR intrinsically more robust against non-reactive perturbations. Crucially, when the total chemical conversion during the monitored reaction period is small—as in the present system—nonlinearities in the relationship between Δf and concentration cannot be averaged out. Even subtle deviations from linear proportionality between Δf and chemical conversion translate into systematic bias in the extracted rate constant. Although normalization by the asymptotic shift ($\Delta\infty$) eliminates trivial scaling errors, it does not compensate for additive drift or concentration-dependent nonlinear response. The resulting bias manifests as an overestimation of the apparent reaction rate and, consequently, an underestimation of the degree of VSC-induced rate suppression.

These findings demonstrate that differential cavity observables provide a quantitatively superior basis for extracting kinetic parameters in VSC-modified reactions. More broadly, they emphasize that methodological artifacts can masquerade as mechanistic effects if the physical origin of the spectroscopic observable is not carefully disentangled from the chemical signal. Establishing robust readout strategies is therefore essential for the reliable interpretation of cavity-controlled chemistry.

Conclusions

In this work, we critically examined the quantitative reliability of cavity-based kinetic readout strategies in vibrational strong coupling experiments. By benchmarking two spectroscopic observables in a prototypical VSC-controlled PTA deprotection reaction, we demonstrate that the choice of cavity observable has a direct and substantial impact on the extracted rate constant. While both Δf and ΔFSR methods capture the qualitative trend of VSC-induced reaction suppression, they yield quantitatively different kinetic parameters. The ΔFSR-based analysis reveals a ~5.1-fold reduction in reaction rate under VSC, whereas the Δf-based approach reports only ~4.25-fold suppression, thereby significantly underestimating the true magnitude of cavity-induced reactivity modulation. This discrepancy arises from the greater susceptibility of single-mode frequency tracking to thermal drift, cavity perturbations, and concentration-dependent nonlinear response. These findings indicate that even modest systematic distortions in spectroscopic readout can translate into substantial underestimation of vacuum-field-induced kinetic effects. Differential cavity observables, such as ΔFSR, intrinsically suppress common-mode perturbations and provide a more faithful representation of refractive-index changes associated with chemical conversion.

Beyond the specific PTA system studied here, our results emphasize that rigorous methodological validation is essential for the reliable interpretation of cavity-modified chemistry. Establishing robust kinetic readout strategies is critical for advancing the quantitative foundation of vibrational strong coupling and for distinguishing genuine cavity-induced reactivity changes from measurement-induced artifacts. When endpoint sampling is feasible, cross-validation using independent analytical techniques, such as GC, NMR, or HPLC, is generally encouraged.[32] Nevertheless, time-resolved sampling in conventional static FP microcavities remains challenging because of the limited cavity volume and the risk of disturbing the VSC condition during sampling. Recently developed continuous-flow FP-cavity systems provide a promising methodological route to overcome this limitation by expanding the reaction volume and enabling controlled residence-time measurements.[33] Future integration of such flow-based VSC platforms with independent analytical methods may provide a more comprehensive strategy for validating cavity-modified reaction kinetics.

Author contributions

F. Z. and R. P. designed and conceptualized the study. K. G. and X. Z. performed the investigations. K. G. and X. Z. provided the materials and methods. K. G., X. Z., R. P. and F. Z. analyzed the data. K. G., R. P. and F. Z. wrote the original draft of the paper. All authors discussed the results, reviewed, edited and contributed to the final paper. K. G. and X. Z. contributed equally.

Conflicts of interest

There are no conflicts to declare.

Data availability

The supporting data has been provided as part of the supplementary information (SI). Supplementary information is available. See DOI: https://doi.org/10.1039/d6ra01794k.

Acknowledgements

This work was supported by the National Nature Science Foundation of China (No. T2241002, 32271298, 62275157), the National Key Research and Development Program of China (No. 2021YFA1200402), the Opening Grants of Innovation Laboratory of Terahertz Biophysics (No. 23-163-00-GZ-001-001-02-01), and Wenzhou Institute of the University of Chinese Academy of Sciences (WIU-CASQD2021003, WIU-CASQD20210011, WIU-CASQD2023024).

References

1 T. W. Ebbesen, *Acc. Chem. Res.*, 2016, **49**, 2403–2412.
2 J. Lather, P. Bhatt, A. Thomas, T. W. Ebbesen and J. George, *Angew. Chem., Int. Ed.*, 2019, **58**, 10635–10638.
3 A. Thomas, J. George, A. Shalabney, M. Dryzhakov, S. J. Varma, J. Moran, T. Chervy, X. Zhong, E. Devaux,

C. Genet, J. A. Hutchison and T. W. Ebbesen, *Angew. Chem., Int. Ed.*, 2016, **55**, 11462–11466.
4 T. E. Li, A. Nitzan and J. E. Subotnik, *Nat. Commun.*, 2022, **13**, 4203.
5 G. Yin, T. Liu, L. Zhang, T. Sheng, H. Mao and W. Xiong, *Science*, 2025, **389**, 845–848.
6 A. Jayachandran, B. Patrahau, J. G. Ricca, M. K. Mahato, Y. Pang, K. Nagarajan, A. Thomas, C. Genet and T. W. Ebbesen, *Angew. Chem., Int. Ed.*, 2025, **64**, e202503915.
7 Y. Tang, G. M. Andolina, A. Cuzzocrea, M. Mezera, P. B. Szabó, Z. Schätzle, F. Noé and P. A. Erdman, *J. Chem. Phys.*, 2025, **163**, 034108.
8 A. Thomas, E. Devaux, K. Nagarajan, T. Chervy, M. Seidel, G. Rogez, J. Robert, M. Drillon, T. T. Ruan, S. Schlittenhardt, M. Ruben, D. Hagenmüller, S. Schütz, J. Schachenmayer, C. Genet, G. Pupillo and T. W. Ebbesen, *J. Chem. Phys.*, 2025, **162**, 134701.
9 A. Cargioli, M. Lednev, L. Lavista, A. Camposeo, A. Sassella, D. Pisignano, A. Tredicucci, F. J. Garcia-Vidal, J. Feist and L. Persano, *Nanophotonics*, 2024, **13**, 2541–2551.
10 R. Arul, D.-B. Grys, R. Chikkaraddy, N. S. Mueller, A. Xomalis, E. Miele, T. G. Euser and J. J. Baumberg, *Light: Sci. Appl.*, 2022, **11**, 281–290.
11 W. Ahn, J. F. Triana, F. Recabal, F. Herrera and B. S. Simpkins, *Science*, 2023, **380**, 1165–1168.
12 T. E. Li, A. Nitzan and J. E. Subotnik, *J. Chem. Phys.*, 2020, **152**, 234107.
13 J. Lather and J. George, *J. Phys. Chem. Lett.*, 2021, **12**, 379–384.
14 P. A. Thomas, W. J. Tan, V. G. Kravets, A. N. Grigorenko and W. L. Barnes, *Adv. Mater.*, 2024, **36**, 2309393.
15 C. Zhong, S. Hou, X. Zhao, J. Bai, Z. Wang, F. Gao, J. Guo and F. Zhang, *ACS Photonics*, 2023, **10**, 1618–1623.
16 J. Singh, P. Garg, R. V. Anand and J. George, *Chem.–Eur. J.*, 2024, **30**, e202400607.
17 K. Hirai, H. Ishikawa, Y. Takahashi, J. A. Hutchison and H. Uji-i, *Chem.–Eur. J.*, 2022, **28**, e202201260.
18 J. Bai, Z. Wang, C. Zhong, S. Hou, J. Lian, Q. Si, F. Gao and F. Zhang, *Biochem. Biophys. Res. Commun.*, 2023, **652**, 31–34.
19 Q. Si, J. Guo, J. Lian, A. Liu, X. Zhao, S. Liu, R. Peng, R. Xu and F. Zhang, *Chem. Eng. J.*, 2024, **496**, 154197.
20 M. Hertzog and K. Börjesson, *ChemPhotoChem*, 2020, **4**, 612–617.
21 F. Herrera and W. L. Barnes, *Philos. Trans. R. Soc., A*, 2024, **382**, 20230343.
22 C. Muller, R. J. Mayer, M. Piejko, B. Patrahau, V. Bauer and J. Moran, *Angew. Chem.*, 2024, **136**, e202410770.
23 P. A. Thomas and W. L. Barnes, *J. Chem. Phys.*, 2024, **160**, 204303.
24 W. Ying, M. A. D. Taylor and P. Huo, *Nanophotonics*, 2024, **13**, 2601–2615.
25 S. M. Vega, W. Ying and P. Huo, *J. Am. Chem. Soc.*, 2025, **147**, 19727–19737.
26 D. C. Sweeney, A. Birri and C. M. Petrie, *Opt. Express*, 2022, **30**, 29148–29160.
27 M. A. Popović, C. Manolatou and M. R. Watts, *Opt. Express*, 2006, **14**, 1208–1222.
28 J. Lee, J. Kim and K. An, *Sci. Rep.*, 2024, **14**, 3471.
29 M. A. Michon and B. S. Simpkins, *J. Am. Chem. Soc.*, 2024, **146**, 30596–30606.
30 K. Schwennicke, A. Koner, J. B. Pérez-Sánchez, W. Xiong, N. C. Giebink, M. L. Weichman and J. Yuen-Zhou, *Chem. Soc. Rev.*, 2025, **54**, 6482–6504.
31 G. Yin, T. Liu, L. Zhang, T. Sheng, H. Mao and W. Xiong, *Science*, 2025, **389**, 845–848.
32 B. Xiang and W. Xiong, *Chem. Rev.*, 2024, **124**, 2512–2552.
33 J. Lian, Y. Song, Q. Si, X. Zhao, L. Chen, R. Xu and F. Zhang, *ACS Photonics*, 2025, **12**, 3557–3564.